Acta Materialia 200 (2020) 366–377

Contents lists available at ScienceDirect

Acta Materialia

journal homepage: www.elsevier.com/locate/actamat

Full length article

Recrystallization-based grain boundary engineering of 316L stainless steel produced via selective laser melting

Shubo Gao[a], Zhiheng Hu[b], Martial Duchamp[c], P.S. Sankara Rama Krishnan[c], Sravya Tekumalla[a], Xu Song[d], Matteo Seita[a,c,*]

[a] School of Mechanical and Aerospace Engineering, Nanyang Technological University, 50 Nanyang Avenue, 639798, Singapore
[b] Singapore Institute of Manufacturing Technology, 73 Nanyang Drive, 637662, Singapore
[c] School of Materials Science and Engineering, Nanyang Technological University, 50 Nanyang Avenue, 639798, Singapore
[d] Department of Mechanical and Automation Engineering, The Chinese University of Hong Kong, Shatin, N.T. Hong Kong, China

ARTICLE INFO

Article history:
Received 19 August 2020
Revised 23 August 2020
Accepted 4 September 2020
Available online 10 September 2020

Keywords:
Grain boundary engineering
Selective laser melting
Recrystallization
Solidification structure
316L stainless steel

ABSTRACT

Grain boundary engineering (GBE) is a thermomechanical processing strategy to enhance the physical and mechanical properties of polycrystalline metals by purposely incorporating special types of grain boundaries—such as twin boundaries (TB)—in the microstructure. Because of the multiple strain-annealing cycles involved, conventional GBE is not directly applicable to near-net-shape parts, such as those produced via additive manufacturing (AM) technology. In this study, we explore a different GBE processing route that leverages TB multiplication during recrystallization of austenitic 316L stainless steel produced via selective laser melting (SLM). We find that recrystallization requires a minimum level of mechanical deformation, which scales with the laser scanning speed employed during SLM. We ascribe this relationship to the cell size and the amount of solute segregating at cell boundaries during rapid solidification, which are inversely and directly proportional to the laser scanning speed, respectively. The coarser the cell structure and the more uniform the chemical composition, the easier the nucleation and growth of recrystallized grains. Our results provide the groundwork for devising AM-compatible GBE strategies to produce high-performance parts with complex geometry.

1. Introduction

Grain boundary engineering (GBE) encompasses different material processing methods that impart polycrystals with a large number fraction of "special" grain boundaries (GBs), such as twin boundaries (TBs) and other GBs with low energy [1,2]. In metals and metal alloys, GBE results in markedly improved GB-controlled properties, including ductility [3], fatigue [4], corrosion resistance [5], and diffusion [6]. Conventional GBE methods generally involve multiple strain-annealing cycles on plates or sheets of material that are subsequently machined or formed into a final product [7,8].

Because materials undergo copious plastic deformation during these treatments, it is difficult to apply GBE to near-net-shape parts—including those produced by metal additive manufacturing (AM) [9]—without modifying their geometry substantially. However, devising a GBE method that is compatible with AM would enable the direct production of high-performance parts with complex geometry which require minimal follow-on processing. To achieve this goal, different studies have proposed to integrate the mechanical treatments necessary for GBE—such as rolling [10] and peening [11]—during the layer-by-layer AM process, or to selectively add material on parts that already underwent mechanical processing [12]. These hybrid manufacturing strategies, however, pose several challenges that arise from the large and repeated plastic deformations involved, or the thermal stresses that result from the localized heat sources employed, which may change the target geometry substantially or compromise materials properties.

An alternative approach is that of employing specialized heat treatments (HT) to manipulate the GB character distribution (GBCD) in as-built AM parts [13,14]. Previous works have demonstrated that HT used to relieve residual stresses [15], homogenize microstructure [16], or modify phase fractions [17] also have an impact on the GBCD. However, a mechanistic understanding of

---

* Corresponding author.
E-mail address: mseita@ntu.edu.sg (M. Seita).

https://doi.org/10.1016/j.actamat.2020.09.015

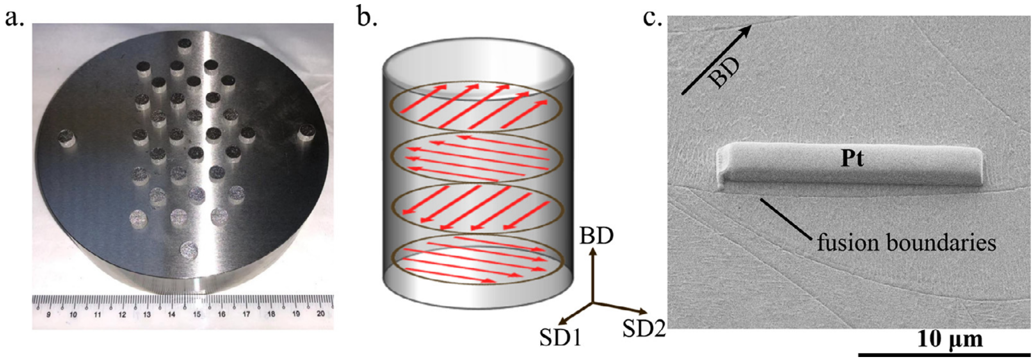

Fig. 1. (a) SLM-produced 316L SS cylinders. (b) Schematic illustration of scanning strategy adopted in the experiments. (c) An electron micrograph showing the location from where TEM lamellae were taken with respect to the melt pool boundary.

Table 1
Chemical composition of the as-received 316L SS powder (in wt%).

Ni	Cr	Mo	Si	Mn	C	P	Cu	Fe
12.60	17.70	2.67	0.73	1.64	0.027	0.010	0.15	Bal.

how the GBCD changes upon HT and as a function of the initial AM microstructure is still lacking.

Here we present a systematic recrystallization study of 316L stainless steel (316L SS) produced by selective laser melting (SLM) to identify a suitable processing route that enables GBE of AM materials in one single iteration—as opposed to using multiple, layer-by-layer straining cycles. In low stacking fault energy metals such as 316L SS, recrystallization leads to copious TB multiplication [18]. We investigate the critical amount of externally applied plastic strain that is required to trigger the recrystallization process and relate it to the TB length fraction in the microstructure. We also study how the laser scanning speed used in the SLM process affects the onset and extent of recrystallization. We find that recrystallization requires a minimum level of mechanical deformation, which scales with the laser scanning speed. After ruling out the effects of residual stress, crystallographic texture, grain size, and geometrically necessary dislocation (GND) density, we ascribe this relationship to the solute-decorated cellular structure that forms during solidification of the alloy, whose size and chemical composition dictates nucleation and growth of recrystallized grains. Decreasing the laser scanning speed gives rise to coarser cells and lower solute segregation, which promote deformation twinning and enable recrystallization at lower strain levels. Our results open the path to GBE of 316L SS parts with improved performance—such as enhanced corrosion resistance [8,19]—using a combination of specific SLM process parameters and post-production HT.

2. Experimental

We produced 316L SS cylindrical specimens (6.0 mm in diameter and 3.3 mm in height) from gas atomized powder with nominal composition shown in Table 1 and particle size ranging from 5 μm to 23 μm. We 3D-printed the specimens (shown in Fig. 1a) using a custom-made SLM machine equipped with a 100 W continuous wave IPG fiber laser with 1070 nm wavelength. We set laser power to 60 W, beam diameter to 15 μm, hatch spacing to 20 μm, powder layer thickness to 10 μm, and a variable scanning speed ranging between 400 mm/s and 800 mm/s. All experiments were carried out in nitrogen atmosphere. We chose a unidirectional scanning strategy in each layer and rotated the scanning direction by 90° after each layer, as shown schematically in Fig. 1b.

We divided all specimens into three batches, which we used for different experiments. The first batch comprised specimens manufactured at constant laser scanning speed of 600 mm/s. We used this first batch to study recrystallization at different macroscopic strain levels (i.e. 0%, 2.7%, 5.4%, 7.7%, 10%, 15%, 20%, 30%, and 40%). The second batch comprised specimens manufactured using 400 mm/s, 600 mm/s, and 800 mm/s as laser scanning speed. We compressed all specimens from this second batch up to 8.6% and 20% strain. We used these samples to investigate changes in recrystallization as a function of laser scanning speed. The third batch consisted of specimens produced at constant volumetric energy density (VED), but different laser power to scanning speed ratio (i.e., 40 W/ 400 mm/s, 50 W/ 500 mm/s and 70 W/ 700 mm/s). We compared the results obtained on this third batch with those of the second batch to decouple the role of VED from that of laser scanning speed on recrystallization.

We carried out all compression tests at a constant strain rate of 1.5 mm/min using an Instron universal testing system. To induce recrystallization, we heat treated the specimens—as-built, as well as those deformed from three batches—at 1050°C for 30 min in an Elite laboratory chamber furnace. This annealing temperature is often used for solution treatment as well as for GBE of stainless steel [5,8,20]. All the HT were followed by air cooling.

We cut the specimens along the cross-section containing the build direction (BD) and laser scan direction (SD1) and prepared the specimen surface following standard metallographic procedures. We characterized the microstructure by means of scanning electron microscopy (SEM) and electron back-scatter diffraction (EBSD) techniques, using a JEOL 7600 field emission microscope. We employed EBSD to assess GB statistics and GND densities using a step-size of 1 μm and 0.5 μm, respectively. We analyzed and plotted the raw EBSD data using the software Channel 5 (by Oxford Instruments) and MTEX 5.3, which is a comprehensive and free MATLAB toolbox for analyzing and plotting crystallographic quantities [21]. We classified GBs according to their misorientation into low angle grain boundaries (LAGBs), high angle grain boundaries (HAGBs), and twin boundaries (TBs). LAGBs range between 2° to 15°, while HAGBs are characterized by a misorientation angle $>15^\circ$. TBs are defined as $\Sigma 3$ coincidence site lattice boundaries with misorientation angle and axis of 60° and $\langle 111 \rangle$, respectively. We used Brandon's criterion to account for slight angular deviations from the nominal TB misorientation $(15^\circ/\sqrt{3} = 8.66^\circ)$ [22]. All GB fractions computed in this work are length fractions. To study the solidification structure of 316L SS, we further etched the polished specimens to make the cells visible under SEM, using a solution of hydrofluoric and nitric acid (HF: HNO_3: H_2O=1:4:45) for 20 min.

We employed X-ray diffraction (XRD) to identify phases and compute residual stresses in the as-built 316L SS specimens as

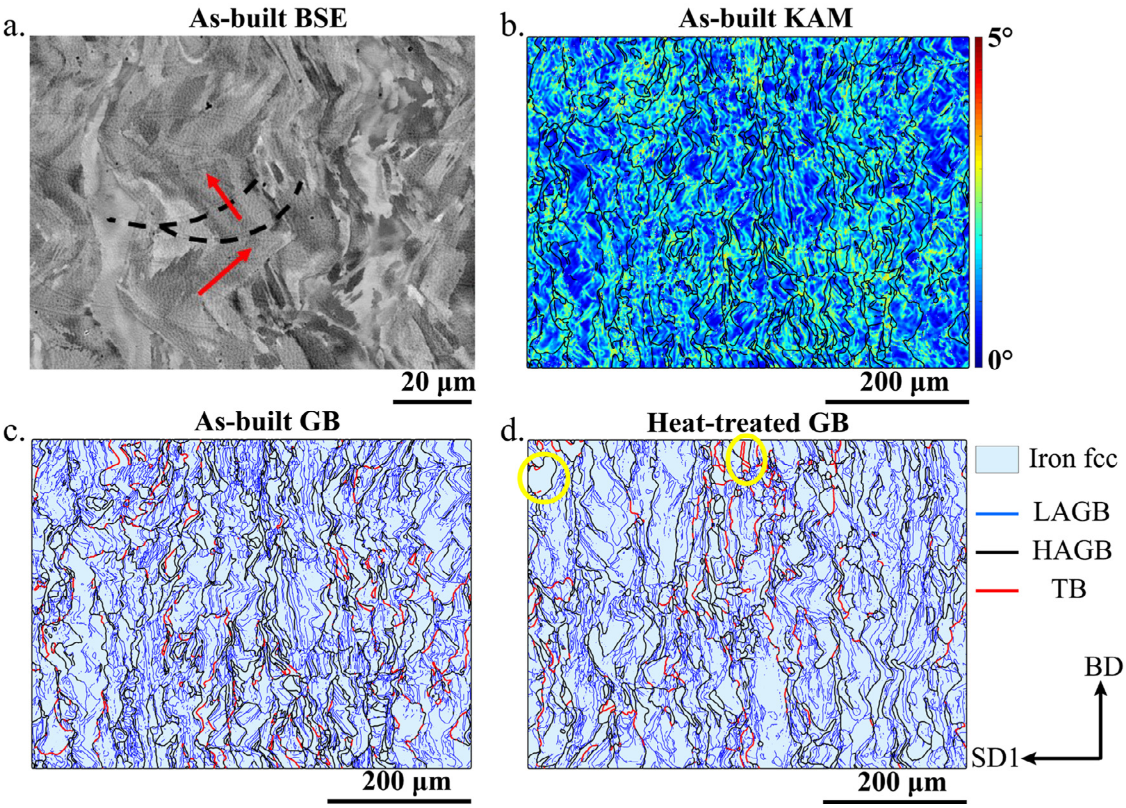

Fig. 2. As-built microstructure of 316L SS produced using a scanning speed of 600 mm/s. (a) High magnification BSE micrograph showing a typical zig-zag grain structure. (b) KAM map computed from the raw EBSD data. (c) and (d) GB maps showing the distribution of LAGBs, HAGBs, and TBs in a representative as-built and heat-treated specimen, respectively.

a function of laser scanning speed. We performed the measurements on an area in the middle of the sample cross-section using an X-Ray diffractometer (Panalytical Empyrean XRD) equipped with a CuKα (λ =1.5406 Å) source at 30 kV. For phase identification, we acquired 2θ scans ranging from 40° to 100° in steps of 0.013°. We computed residual stresses using the 'd vs. $\sin^2 \Psi$' method from (311) planes detected within a 2θ range between 88° and 93° over 10 different tilting angles (Ψ). For the calculation, we set the Young's modulus and Poisson's ratio to 171 GPa and 0.28, respectively.

To characterize the cellular structure in detail and map differences in solute segregation as a function of laser scanning speed in the as-built samples, we carried out energy-dispersive X-ray spectroscopy (EDX) in scanning transmission electron microscopy (STEM) mode using a JEM-GrandARM aberration-corrected transmission electron microscope (TEM) operated at 300 kV. We cut TEM lamellae from the samples by means of a ZEISS Crossbeam 540 focused ion beam (FIB) using gallium as ion source. Because variations in cell growth direction and solidification velocity within individual melt pools may affect the comparison between cell structures in different samples, we cut the TEM lamellae from grains with the same crystallographic orientation (⟨110⟩ parallel to the BD and ⟨001⟩ parallel to SD2) and at the same distance from the melt pool fusion boundaries, as shown in Fig. 1c.

3. Results

3.1. As-built and HT 316L SS microstructure

Fig. 2a shows the back-scattered electron (BSE) micrograph along the BD-SD1 cross section of an as-built specimen produced using a scanning speed of 600 mm/s. We observe zig-zag columnar grains that grow epitaxially across multiple melt pools (some melt pool boundaries are highlighted by the dashed lines in Fig. 2a). This grain morphology is often found in additively manufactured face centered cubic (FCC) metals when employing alternating scanning strategies [23,24], which continuously revert the direction of the thermal gradient across successive layers [25].

Figs. 2b and 2c show the kernel average misorientation (KAM) map and GB network computed from the raw EBSD data on the same cross-section, respectively. The KAM map plots the average misorientation between every pixel and a kernel of surrounding pixels. A visual comparison between these two maps qualitatively suggests that local misorientations coincide with the occurrence of LAGBs, which account for ~70% of all GBs in this microstructure. In addition to those, we measure ~2.3% TBs and ~27.7% HAGBs. Because of the rapid solidification conditions [26], SLM-produced materials often exhibit microstructures consisting of large numbers of LAGBs [27], which form upon coalescence of cells or dendrites that accumulate misorientation as they grow [28,29]. As a result, these regions are rich in GNDs, which provide the strain energy required to drive recrystallization.

We heat treated the as-built specimens to 1050 °C for 30 min to investigate whether the as-built GND density is sufficient to trigger recrystallization. The result, shown in Fig. 2d, indicates that only a few areas (circled in yellow) actually recrystallize, yielding a minor increase in the overall TB fraction from 2.3% to 3.9%. We conclude that the stored strain energy in the as-built alloy is insufficient to trigger complete recrystallization. To increase the amount of stored energy and enable recrystallization during HT, we explore two different routes: (1) mechanically introducing plastic strain into the as-built specimens before HT (batch 1 experiments), and (2) in-

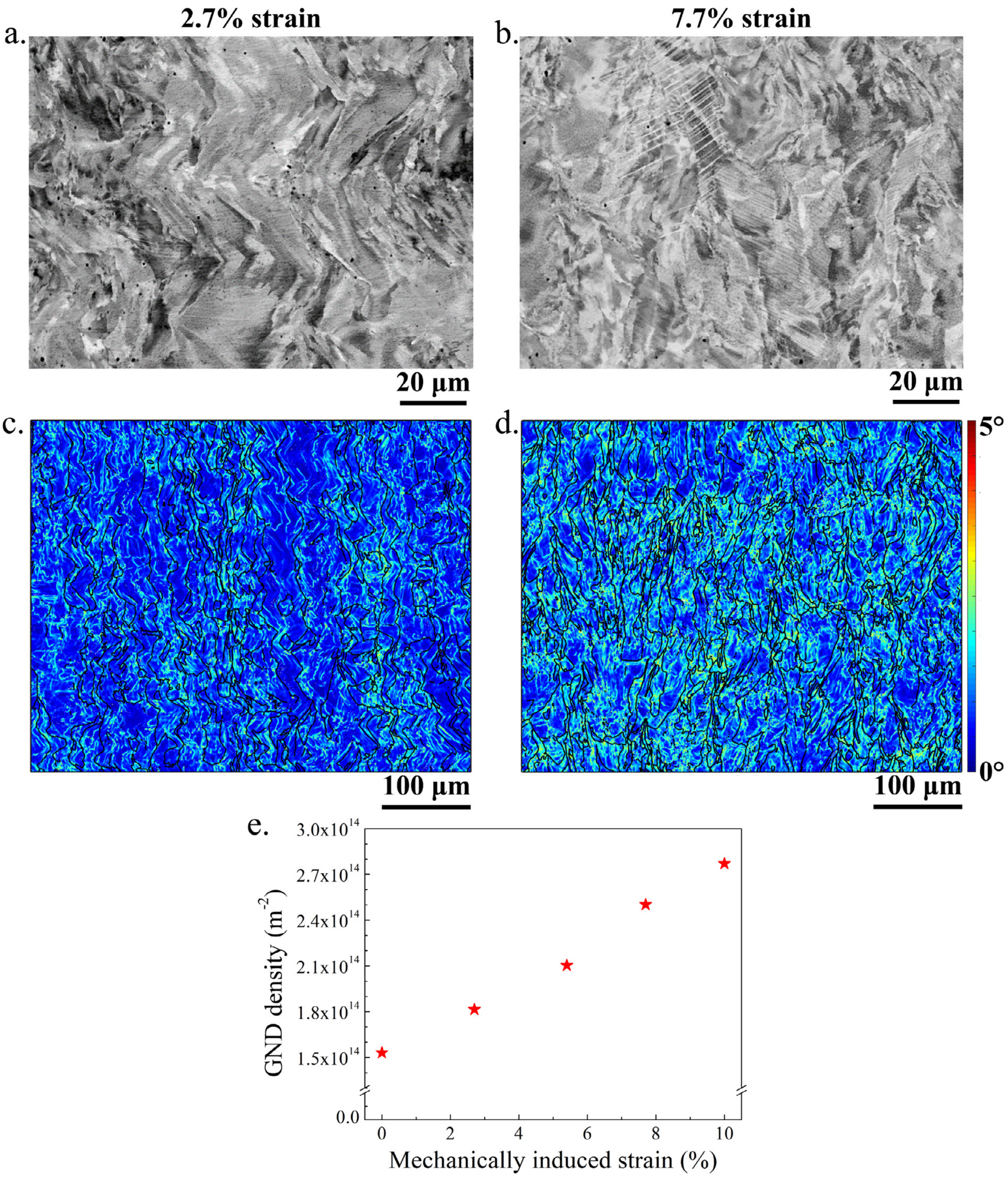

Fig. 3. Deformed 316L SS microstructures: (a) and (b) BSE micrographs and (c) and (d) corresponding KAM maps of samples deformed up to 2.7% and 7.7% strains, respectively. (e) Estimated average GND density as a function of plastic strain.

creasing the initial stored energy by varying SLM process parameters (batch 2 experiments).

3.2. Recrystallization upon plastic deformation

We compress batch 1 specimens to different levels of strain (i.e. 2.7%, 5.4%, 7.7%, 10%, 15%, 20%, 30%, and 40%) and investigate the corresponding fraction of recrystallized microstructure and TB fraction. The BSE micrographs in Fig. 3 show distinct differences in the deformed microstructure depending on the applied strain. At 2.7% strain (Fig. 3a), we observe no obvious difference from the as-built microstructure (Fig. 2a), since the dominant deformation mechanism is dislocation slip. As the external strain increases to 7.7%, however, we observe deformation twinning (Fig. 3b). The KAM maps corresponding to these two strain levels are shown in Figs. 3c and 3d, respectively. Qualitatively, we observe a denser and more uniform orientation spread across the specimen surface as the strain level increases. To convert local misorientation into GND density, we use [30]:

$$\rho = \frac{\alpha\theta}{Xb} \tag{1}$$

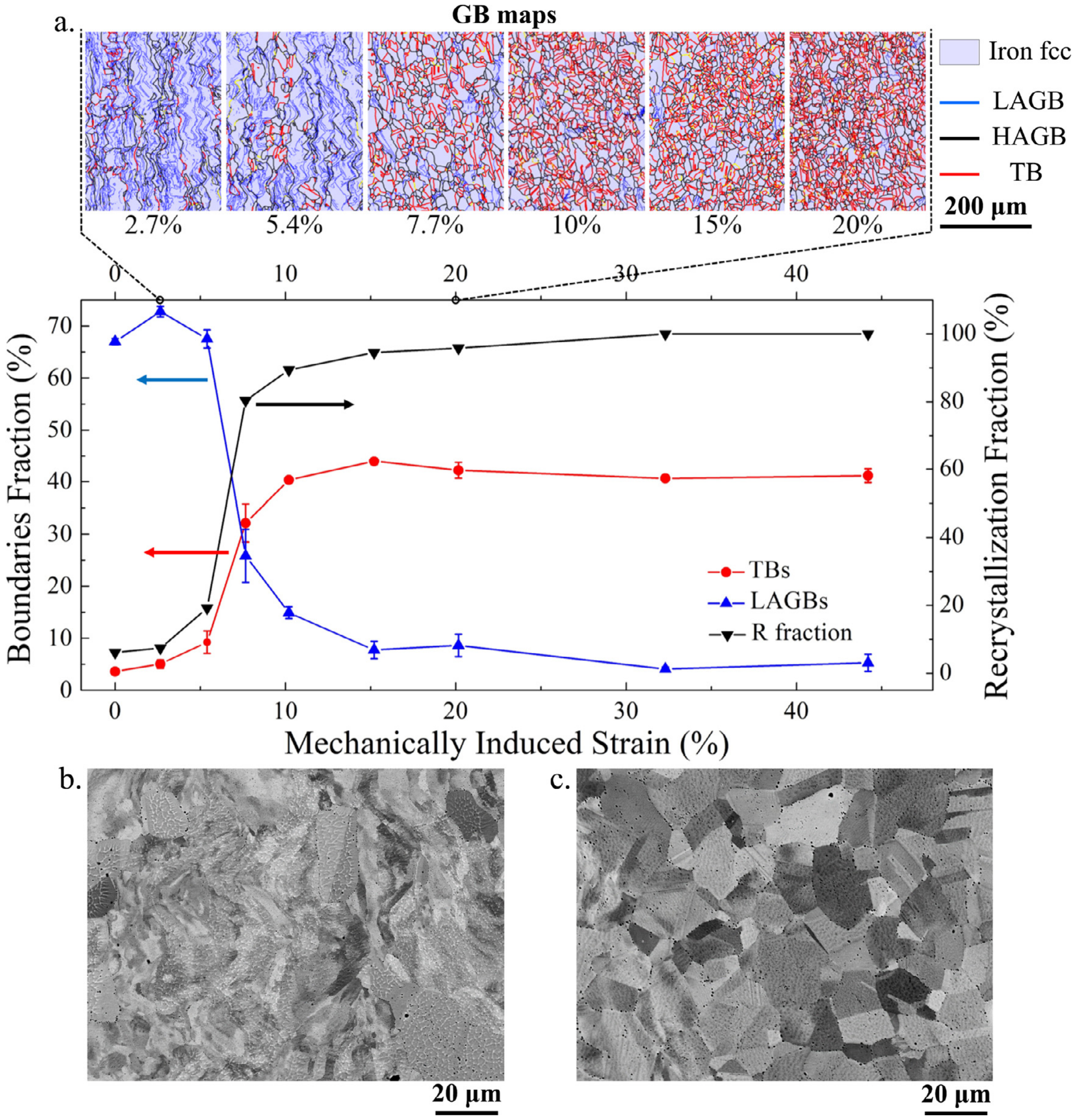

Fig. 4. (a) GB maps and GBCD/recrystallization analysis of the GBE batch 1 specimens. (b) and (c) high magnification BSE micrographs of GBE specimens strained at 5.4% and 20%, respectively.

Here, $\alpha=2$ for LAGB (tilt boundaries), θ is the local misorientation angle, X corresponds to the EBSD scan step-size used to compute the KAM map, and b is the magnitude of Burgers vector. Using Eq. (1), we plot the average GND density versus strain level (from 0% to 10%) in Fig. 3e. In the as-built microstructure (0% strain), the estimated average GND density equals $1.5 \times 10^{14}\ m^{-2}$, which is comparable to that typically found in lightly deformed or ice-quenched FCC metals [31-33]. As the mechanically induced strain increases, the average GND density grows up to $2.8 \times 10^{14}\ m^{-2}$, about twice that estimated in the as-built material. Because of the distorted lattice in highly strained specimens, we could not characterize specimens deformed beyond 10% strain by means of EBSD.

We annealed the compressed specimens from batch 1 using the same HT detailed in Section 3.1 and assessed the GBCD in the resulting GBE specimens by means of EBSD. Fig. 4a plots the fractions of recrystallized microstructure, LAGB, and TB for all GBE specimens. All curves show major changes in the microstructure between 5% and 15% strain. Beyond 15% strain, the GBCD reaches a plateau with a TB fraction of ~40%. The EBSD GB map of the GBE specimen strained up to 20% shows a completely recrystallized microstructure comprising uniformly distributed TBs and equiaxed grains with average size of 10 µm (Fig. 4c). Conversely, at lower strain levels we find patches of recrystallized areas with high TB content surrounded by a columnar microstructure that is rich in LAGBs (Fig. 4b) and that is similar to the one found in as-built specimens (Fig. 2a).

Interestingly, the inflection point in the GBCD and recrystallization curves is around 7% strain, which matches the onset of deformation twinning we observe from the BSE micrographs in Fig. 3b. Taken holistically, the results presented in Fig. 4 suggest that recrystallization in SLM-produced specimens is function of both the GND density—which can be controlled via mechanical deformation—as well as the presence of deformation twins in the microstructure. The latter are barriers to dislocation motion upon further deformation and thus increase local misorientation, which facilitates nucleation of recrystallized grains [34,35]. While 7.7% strain produces deformation twins in our SLM specimens, it does not yield sufficiently large GND densities to complete the recrystal-

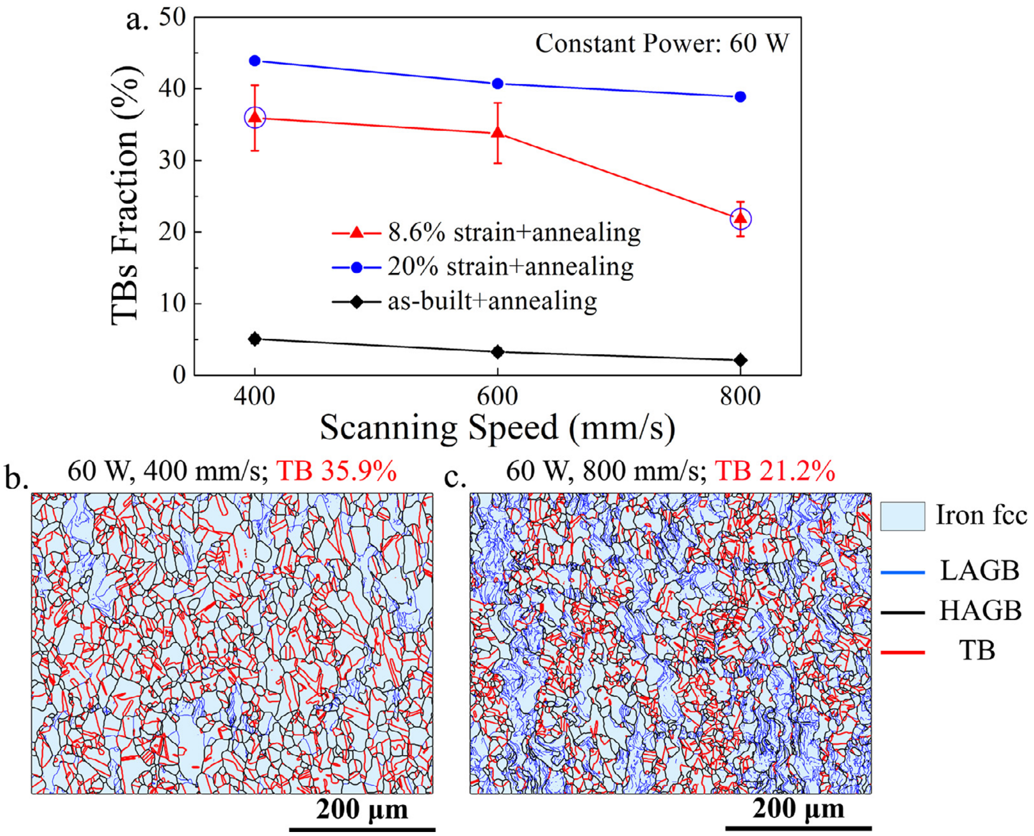

Fig. 5. (a) TB fraction versus scanning speed in SLM-produced 316L SS after GBE involving 0%, 8.6%, and 20% strain. Representative GB maps for GBE specimens produced using (b) 60 W/ 400 mm/s and (c) 60 W/ 800 mm/s and strained up to 8.6%.

lization process. Larger deformations overcome this limitation, but they cause significant deviations from the target geometry, which are difficult to compensate in an actual AM process. In the following section, we explore other strategies to increase GND densities at lower strains and compromise between recrystallization and deformation.

3.3. *Influence of AM parameters on GBE*

The results presented in Section 3.2 are function of the microstructure of batch 1 specimens. In other words, the strain threshold beyond which we achieve full recrystallization depends on the GBCD and inherent GND density generated during that specific SLM process. To investigate the connection between SLM process parameters and the onset and extent of recrystallization, we perform similar GBE experiments on two additional batches of specimens, which we produced using different SLM parameters.

Fig. 5 shows how the TB fraction changes in three sets of SLM 316L SS specimens produced using constant laser power (60 W) but variable laser scanning speed (400 mm/s, 600 mm/s, and 800 mm/s). Under all three GBE conditions (0%, 8.6%, and 20% strain) we find that a slower scanning speed yields larger TB fraction. In both the as-built (0% strained) and 20% strained GBE specimens (the black and blue curves in Fig. 5a), we record minor differences in TB fraction as a function of scanning speed. Conversely, the TB fraction varies significantly as a function of laser scanning speed when deforming the specimens up to 8.6% strain (the red curve in Fig. 5a). The TB fraction in this set of samples reaches a maximum of ~36% at the slowest laser scanning speed (400 mm/s), while it decreases to ~21% as the scanning speed is doubled. Noteworthy is that the relative increase in TB fraction from 400 mm/s to 800 mm/s when compressing the specimens up to 20% (the blue curve) is only marginal compared to what we measure in 8.6% strained specimens (the red curve). In other words, the effect of laser scanning speed on recrystallization is more significant at low strain levels—which are more suitable for GBE of near-net-shape materials. These differences are also evident by comparing the GB maps in Figs. 5b and 5c.

Because we kept laser power constant during SLM of batch 2 specimens, the nominal VED value—which is proportional to the ratio of laser power to laser scanning speed [36]—decreases with increasing scanning speed. To confirm that the recrystallization behavior of SLM 316L SS shown in Fig. 5 is dictated by the laser scanning speed rather than by the energy input, we repeated our GBE experiments (up to 10% strain) on a third batch of specimens comprising three sets of samples produced using a constant VED of 500 J/mm^3, but variable laser scanning speed of 400 mm/s, 500 mm/s, and 700 mm/s. The EBSD GB maps and corresponding TB fractions shown in Fig. 6 confirm the same trend found in batch 2; namely that lower scanning speed leads to a higher recrystallization fraction.

3.4. *Effect of laser scanning speed on the as-built microstructure*

To unveil the mechanisms governing recrystallization of SLM 316L SS, we analyze the microstructural features which are known to affect this process—including GND density, phase content, residual stresses, crystallographic texture, grain size, and solidification structure—and compare them in the two specimens that exhibit the most extreme differences in recrystallization behavior; namely those produced using a 400 mm/s and 800 mm/s laser scanning speed (see Fig. 5).

We use the EBSD data to compute the GND density in the as-built samples (i.e. 0% strain) similar to what we present in

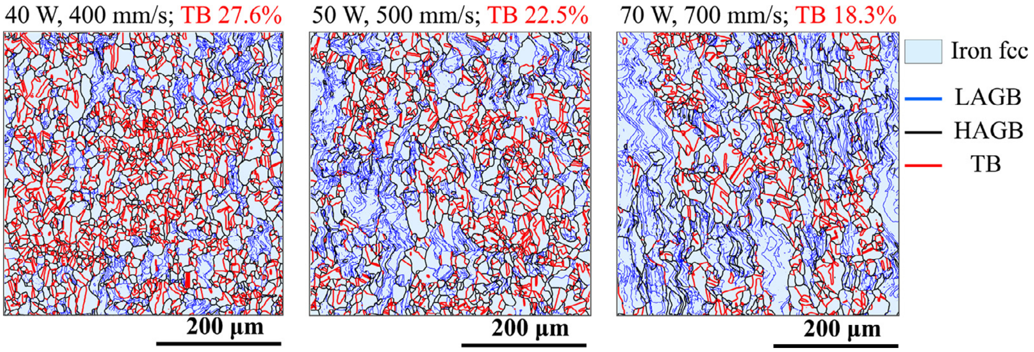

Fig. 6. Representative GB maps for GBE specimens produced using a constant VED of 500 J/mm^3 but variable laser scanning speed.

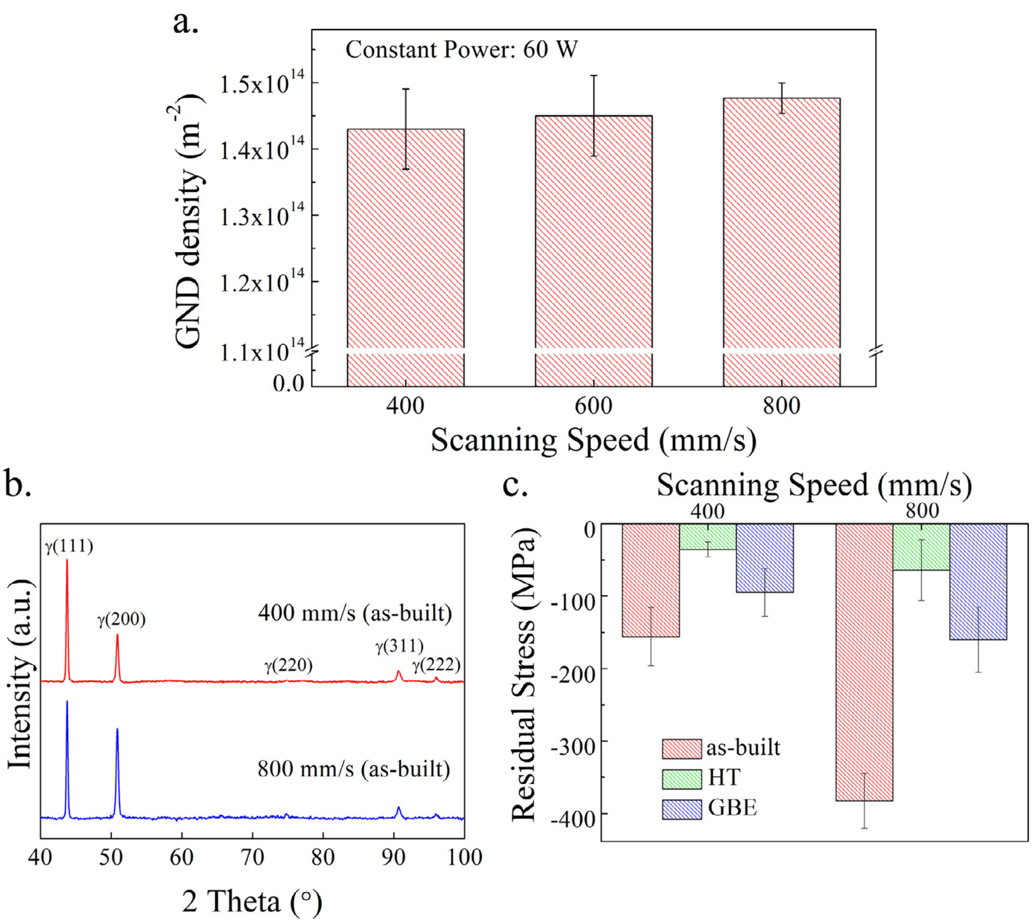

Fig. 7. (a) Computed average GND densities in as-built 316L SS specimens as a function of laser scanning speed. (b) XRD patterns of as-built 316L SS produced by 400 mm/s and 800 mm/s. (c) XRD residual stress analysis on as-built, HT, and GBE 316L SS produced by 400 mm/s and 800 mm/s.

Section 3.2 and note that it increases slightly with laser scanning speed (Fig. 7a). This result is consistent with previous findings, which correlate slower scanning speeds with slower cooling rates [37,38] and thus lower GND densities [39,40]. The minor changes in GND density across the three sets of samples may come from the fact that all specimens were produced using the same laser power (60 W). A slower scanning speed in these experiments leads to a higher energy input, which may also contribute to the generation of GNDs [41] by inducing larger volume shrinkage upon solidification of the melt pool [42]. To decouple the effects of laser scanning speed from VED on GND density, we carry out the same analysis on batch 3 specimens (produced at constant VED but variable laser scanning speed). We find a similar trend to that shown in Fig. 7a, with GND densities going from ~ $1.25 \times 10^{14}\ m^{-2}$ to ~ $1.56 \times 10^{14}\ m^{-2}$ in specimens produced using laser power to laser scanning speed ratio of 40 W/400 mm/s and 70 W/700 mm/s, respectively.

The XRD patterns taken from the two specimens indicate no differences in phase content and that both samples are made of austenitic 316L SS (Fig. 7b). It is known that a high laser scanning speed in SLM alloys may result in significant residual stress owing to the high local cooling rates involved [43]. Our XRD measurements confirm this trend, with the specimen produced using a laser scanning speed of 800 mm/s showing higher compressive residual stress than that produced at 400 mm/s. Upon HT (i.e. without applying any mechanical deformation), we record ~75%

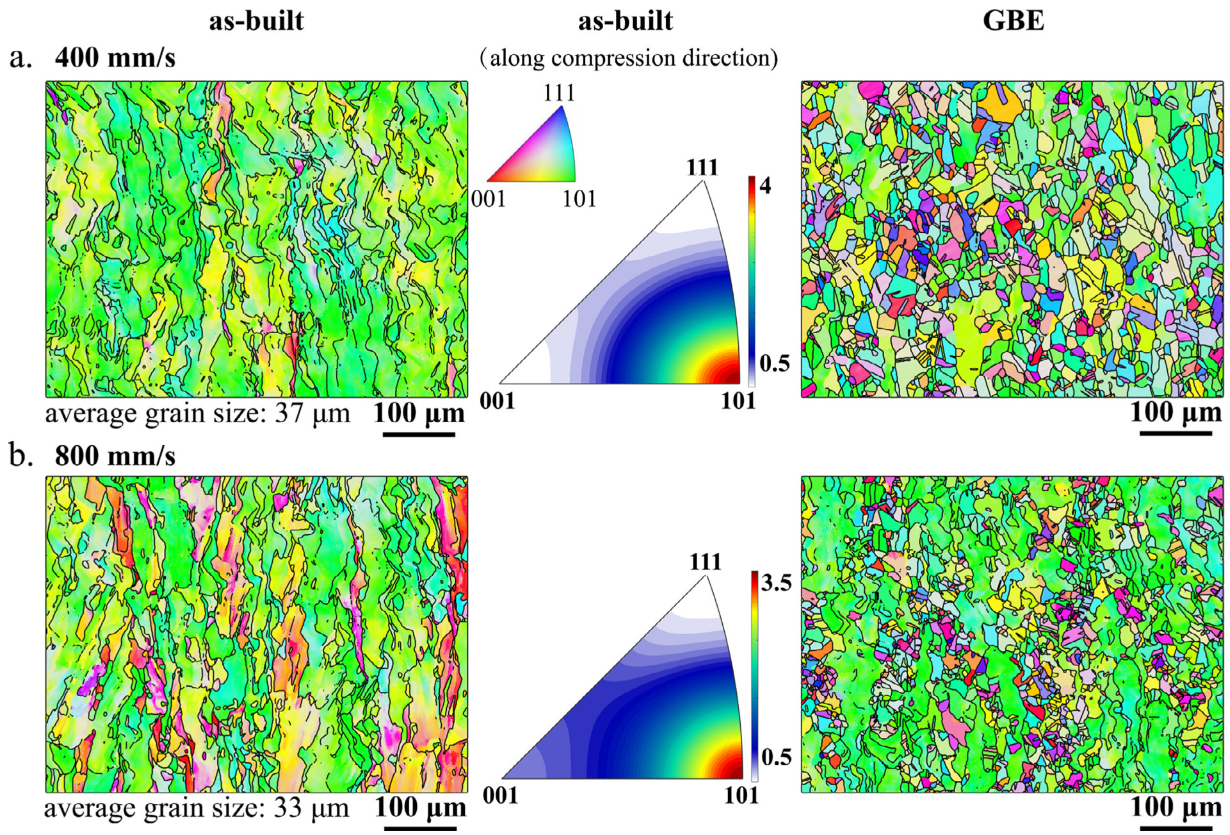

Fig. 8. As-built grain orientation maps, inverse pole figures and GBE grain orientation maps along compression direction of 316L SS using (a) 400 mm/s and (b) 800 mm/s.

and ~90% stress relaxation in the specimens when using a slow and fast laser scanning speed, respectively. We find the same trend after performing GBE involving 8.6% mechanical strain.

Fig. 8 shows the crystallographic texture analysis found in the as-built specimens by means of EBSD. Both samples exhibit a strong ⟨101⟩ texture along the BD, which is commonly seen in SLM 316L SS [24]. An additional, minor ⟨001⟩ texture component is visible in the specimen produced using a laser scanning speed of 800 mm/s. From the as-built grain maps in Fig. 8, we compute an average grain size of ~37 μm and ~33 μm in the specimens produced using a slow and fast laser scanning speed, respectively. The grain maps from the GBE specimens (strained up to 8.6%) shown in Fig. 8 correspond to the GB maps presented in Figs. 5b and 5c. A visual comparison between these two figures suggests that all non-recrystallized areas consist of ⟨101⟩ textured grains.

Fig. 9 shows the STEM and SEM analysis of the cellular structure found in specimens produced using different laser scanning speed. These structures are the results of constitutional undercooling during rapid solidification [44], and are commonly observed in metal alloys produced by SLM [45]. EDX-STEM on the specimens produced using a laser scanning speed of 400 mm/s and 800 mm/s show that cell boundaries are depleted in iron (Fe) and rich in chromium (Cr) and molybdenum (Mo) (Fig. 9a and 9b, respectively). This result is consistent with previous works on SLM of 316L SS [27,46] and is attributed to the larger partition coefficient of Cr and Mo [47], which segregate at the solid/liquid interface during rapid solidification [48]. Interestingly, we measure a significantly different Cr and Mo to Fe ratios at cell boundaries in the two specimens. By taking line-scans across six cell boundaries, we compute a Cr/Fe and Mo/Fe X-ray intensity ratios that are respectively ~20% and ~70% higher at cell boundaries than in the cell interior in the specimen produced using 800 mm/s laser scanning speed. Conversely, the intensity ratios in the sample produced using 400 mm/s laser scanning speed are, respectively, around 10% and 30%. larger at the cell boundaries compare to the cell interior ratios.

Because of the higher resistance to chemical attack brought about by Cr and Mo, the solute-decorated cell boundaries protrude from the surface of chemically etched samples, making the cellular structure readily visible by SEM (Fig. 9c). We compute the average cell size in the SLM 316L SS specimens produced at different laser scanning speeds to be 450 nm at 400 mm/s, 420 nm at 600 mm/s, and 320 nm at 800 mm/s. To ease the comparison of cell size across the three specimens, we select grains of similar crystallographic orientation (i.e. ⟨110⟩ parallel to the BD and ⟨111⟩ parallel to SD2). These results are in line with the common understanding that a fast laser scanning speed leads to high cooling rate and thus finer cellular structure [9]. Using the cell spacing values, λ (μm), measured by SEM, we estimate the cooling rate, $\dot{T}$, in stainless steel following the empirical relationship $\lambda = 80 \cdot \dot{T}^{-0.33}$ [49,50]. We find cooling rates of the order of 2×10^7 K/s and 6×10^6 K/s in specimens produced using 800 mm/s and 400 mm/s laser scanning speed, respectively.

4. Discussion

Both stored energy deriving from the accumulation of dislocations and local strain gradients are required to trigger recrystallization [34]. As-built metal specimens produced by SLM typically exhibit large numbers of dislocations that are uniformly distributed across the volume [27,46]. These dislocations, however, are for the most part statistically stored dislocations [27,51], which—by contrast to GNDs—do not generate lattice misorientation [52,53] and thus do not contribute to the nucleation of recrystallized grains. That is the reason why as-built specimens show <5% TB fraction and negligible recrystallization upon HT (Fig. 2d).

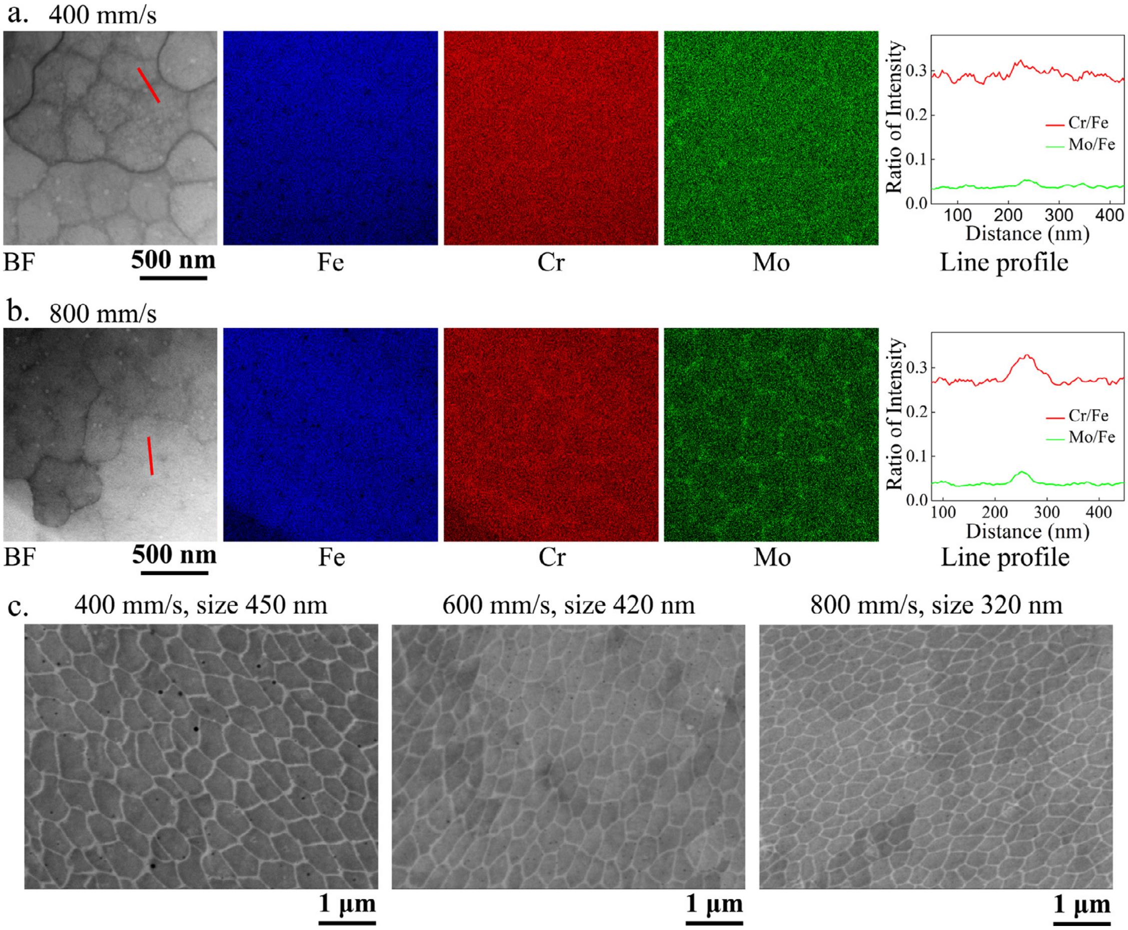

Fig. 9. STEM-EDX results showing the chemical compositions and distribution of segregation cells in (a) 400 mm/s and (b) 800 mm/s. The line profiles shown in the right column correspond to the marked line of the Cr/Fe and Mo/Fe integrated X-ray intensity ratios. (c) Secondary electron micrographs showing the cellular structures in grains with same crystallographic orientation from SLM 316L SS produced using a scanning speed of 400 mm/s, 600 mm/s and 800 mm/s.

To study the recrystallization process in SLM-produced 316L SS, we performed a series of compression tests using increasingly larger strains (Fig. 4). Mechanical deformation both raises the driving force for recrystallization—by increasing the GND density—and provides local strain gradients required to nucleate recrystallized grains—by introducing deformation twins, which act as barriers to dislocation slip and thus lead to local dislocation accumulation [54,55]. Our results indicate that deformation twinning becomes an available deformation mechanism at strain levels around 7.7%. However, only ~80% of a GBE 316L SS specimen strained up to 7.7% recrystallizes, leading to a TB fraction of ~32%. This result suggests that the stored energy in the 7.7% strained microstructure is insufficient to drive full recrystallization.

To investigate how to increase the recrystallized fraction of 316L SS without relying on further mechanical deformation, we produced a second batch of specimens using different laser scanning speed. We find that the recrystallized fraction is highest in GBE specimens produced using a slower scanning speed (Fig. 5). This trend is particularly obvious at lower strain levels; highlighting the opportunity to engineer the GBCD of alloys produced by AM without extensive mechanical deformation. To elucidate the mechanisms governing recrystallization of SLM 316L SS, and to understand the role of laser scanning speed on the GBE process, we analyze the differences in microstructure between the specimens which exhibit the most distinct recrystallization behavior; namely those produced using 400 mm/s and 800 mm/s laser scanning speed. The results, which we report in Section 3.4, point at the cellular structure—namely the cell size and the extent of solute segregation at cell boundaries—as the determining factor governing the recrystallization process. Fig. 9 shows that a faster laser scanning speed yields finer cells and higher solute trapping at cell boundaries. The latter is caused by the shorter time available for solute to diffuse out of the cell boundary into the Fe matrix, and is typically associated with faster solidification rates [56]. This solute-segregation network has been shown to significantly hinder recrystallization nucleation [57,58] and slow down GB migration [59,60]. The denser and richer in solute the network, the higher the driving force required for recrystallization. Thus, the finer and “stronger” solute-segregation cellular structure found in the specimen produced using 800 mm/s laser scanning speed yields limited recrystallization.

Another effect brought about by the segregation of solute in rapidly solidified alloys is the propensity of the alloy to undergo deformation twinning upon mechanical straining, which—as we show in Section 3.2—is propaedeutic for GBE of SLM 316L SS. On the one hand, local variations of chemical composition may affect the alloy stacking fault energy (SFE) and deformation mechanism [61]. Indeed, low SFE materials are more prone to undergo deformation twining rather than cross-slip owing to the restricted dislocation motion caused by the presence of stacking faults. On the other hand, the solute-decorated cell boundaries can act as dislocation sinks and may be able to accommodate large strains [27], thus increasing the critical stress necessary for twinning and hindering the formation and growth of deformation twins [62]. In Fe-Cr-Ni stainless steels, such as that which we use in this study, the SFE is susceptible to the Mo content in the alloy [61,63]. Because Mo

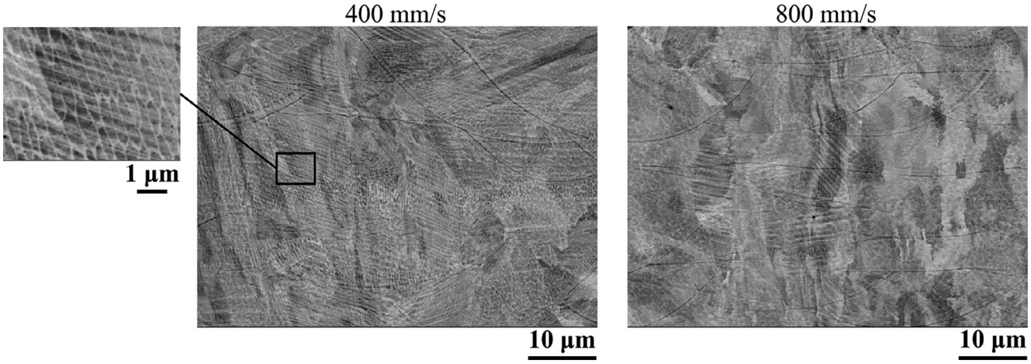

Fig. 10. BSE micrographs of 8.6% strained specimens produced using laser scanning speed of 400 mm/s and 800 mm/s. A visual comparison between the two micrographs suggests a higher number of deformation twins in the sample produced using a slower scanning speed.

concentration in the matrix slightly decreases with increasing laser scanning speed (Fig. 9a and 9b), we would expect to find higher number of deformation twins in samples produced using a laser scanning speed of 800 mm/s. By contrast, we qualitatively observe a larger fraction of deformation twins in specimens produced using slower laser scanning speed (Fig. 10). This evidence suggests that a finer and “stronger” solute-segregation cellular structure hinders deformation twinning and retards the onset of recrystallization.

Therefore, we conclude that the fraction of recrystallized material—and thus the TB fraction—in GBE specimens produced using a scanning speed of 400 mm/s and strained up to 8.6% is the highest (Fig. 5b) because of the combined presence of larger number of deformation twins, which facilitate the nucleation of recrystallized grains, and a “weaker” and sparser solute-segregation network, which does not hinder grain growth.

Noteworthy is that the TB fractions measured in the specimens produced at different laser scanning speeds and strained up to 8.6% (the red curve in Fig. 5a) follow the same trend found in the corresponding average cell size measurements (Fig. 9c). Specifically, the specimens produced at 400 mm/s and 600 mm/s have similar TB fraction and cell spacing, which are both larger than those in the specimens produced at 800 mm/s. Another interesting observation is that the recrystallization hindrance brought about by the solute-segregation network becomes less significant as GBE specimens are deformed up to higher strain levels (Fig. 5a). We speculate that this effect stems from the larger GND density and more activated deformation twinning introduced in all specimens produced using respective scanning speed at strains as large as 20%, which can overcome the effects of the solute-segregation network on deformation twinning and the growth of recrystallized grains. Conversely, the GND densities and the amount of deformation twins in the as-built samples are not large enough to drive full recrystallization. Interestingly, the GND density increases with laser scanning speed (Fig. 7a). Thus, the recrystallization trends illustrated in Fig. 5 cannot be attributed solely to differences in stored energy deriving from GND densities since these two quantities are anticorrelated.

Other possible factors influencing recrystallization include alloy phase content, residual stress, grain size, and crystallographic texture. In our experiments, however, none of these features scales inversely with laser scanning speed and thus may be used to explain the recrystallization behavior shown in Fig. 5. The XRD measurements reported in Fig. 7 show no change in phase content as a function of laser scanning speed. While we expect residual stress to contribute to the recrystallization process [14,64], we measure larger compressive residual stress and larger stress relaxation in specimens produced using fast laser scanning speed, which—after GBE—exhibit lowest recrystallization and TB fraction. A similar anticorrelation exists between average grain size and recrystallization of our specimens. Fine-grained microstructures are more prone to recrystallization owing to the higher number of GBs, which act as nucleation sites [34]. However, our EBSD measurements show slightly smaller average grain size in specimens produced using a laser scanning speed of 800 mm/s (Fig. 8). These specimens also exhibit a number of grains oriented with their ⟨001⟩ axis parallel to the BD, which disrupt the prevailing ⟨101⟩ texture and which are missing in specimens produced using 400 mm/s laser scanning speed. Because of the elastic anisotropy of 316L SS [65], ⟨001⟩ grains are more prone to store strain energy upon deformation compared to ⟨101⟩ grains [27]. As a result, ⟨001⟩ grains recrystallize more easily upon GBE, as confirmed by comparing the EBSD maps in Fig. 8 and Fig. 5. However, the higher recrystallization rate in specimens produced using a laser scanning speed of 800 mm/s does not translate into a larger recrystallization volume.

Our work suggests that gaining control over the solute-segregation network in SLM alloys may be the key to fully recrystallize the microstructure and maximize the TB fraction even at lower strain levels compared to those employed in our experiments. This capability would open the path to producing GBE-AM parts with enhanced properties and optimized geometry for structural applications using novel hybrid AM technologies that combine layer-wise additive and mechanical deformation processes. Another interesting opportunity that emerges from our experiments is that of integrating dissimilar microstructures—comprising of both textured, columnar as well as randomly textured, equiaxed grains—within the same part, as shown in Fig. 5c. Gaining control over the distribution and arrangement of such microstructures could impart unique mechanical behavior or combine properties that are mutually exclusive in monolithic materials [66,67].

Declaration of competing interest

The authors declare that they have no known competing financial interests or personal relationships that could have appeared to influence the work reported in this paper.

Acknowledgement

The authors would like to acknowledge Kai Chen and Karl P. Davidson for valuable discussions and advice, Karl A. Sofinowski for reviewing the manuscript, the Singapore Institute of Manufacturing Technology for providing the 3D printing facility, and NTU for providing access to materials characterization facilities. The authors acknowledge the Facilities for Analysis, Characterization, Testing and Simulations (FACTS) at NTU for access to electron microscopy equipments. This research was funded by the National Research Foundation (NRF) Singapore, under the NRF Fellowship program (NRF-NRFF2018–05) and by the Agency for Science, Technology and Research (A*STAR), under the AME programmatic grant (SMAP, grant No A18B1b0061).

References

[1] V. Randle, Twinning-related grain boundary engineering, Acta Mater 52 (14) (2004) 4067–4081.
[2] T. Watanabe, Grain boundary engineering: historical perspective and future prospects, J Mater Sci 46 (12) (2011) 4095–4115.
[3] E.M. Lehockey, G. Palumbo, K.T. Aust, U. Erb, P. Lin, On the role of intercrystalline defects in polycrystal plasticity, Scr Mater 39 (3) (1998) 341–346.
[4] Y. Gao, R.O. Ritchie, M. Kumar, R.K. Nalla, High-cycle fatigue of nickel-based superalloy ME3 at ambient and elevated temperatures: role of grain-boundary engineering, Metallurgical and Materials Transactions A 36 (12) (2005) 3325–3333.
[5] M. Shimada, H. Kokawa, Z.J. Wang, Y.S. Sato, I. Karibe, Optimization of grain boundary character distribution for intergranular corrosion resistant 304 stainless steel by twin-induced grain boundary engineering, Acta Mater 50 (9) (2002) 2331–2341.
[6] H. Ma, F. La Mattina, I. Shorubalko, R. Spolenak, M. Seita, Engineering the grain boundary network of thin films via ion-irradiation: towards improved electromigration resistance, Acta Mater 123 (2017) 272–284.
[7] M. Kumar, W.E. King, A.J. Schwartz, Modifications to the microstructural topology in f.c.c. materials through thermomechanical processing, Acta Mater 48 (9) (2000) 2081–2091.
[8] R. Jones, V. Randle, Sensitisation behaviour of grain boundary engineered austenitic stainless steel, Materials Science and Engineering: A 527 (16–17) (2010) 4275–4280.
[9] T. DebRoy, H.L. Wei, J.S. Zuback, T. Mukherjee, J.W. Elmer, J.O. Milewski, A.M. Beese, A. Wilson-Heid, A. De, W. Zhang, Additive manufacturing of metallic components – Process, structure and properties, Prog Mater Sci 92 (2018) 112–224.
[10] P.A. Colegrove, J. Donoghue, F. Martina, J. Gu, P. Prangnell, J. Hönnige, Application of bulk deformation methods for microstructural and material property improvement and residual stress and distortion control in additively manufactured components, Scr Mater 135 (2017) 111–118.
[11] N. Kalentics, E. Boillat, P. Peyre, C. Gorny, C. Kenel, C. Leinenbach, J. Jhabvala, R.E. Logé, 3D Laser Shock Peening – A new method for the 3D control of residual stresses in Selective Laser Melting, Mater Des 130 (2017) 350–356.
[12] M. Bambach, I. Sizova, B. Sydow, S. Hemes, F. Meiners, Hybrid manufacturing of components from Ti-6Al-4 V by metal forming and wire-arc additive manufacturing, Journal of Materials Processing Technology 282 (2020) 116689.
[13] S. Holland, X. Wang, X.Y. Fang, Y.B. Guo, F. Yan, L. Li, Grain boundary network evolution in Inconel 718 from selective laser melting to heat treatment, Materials Science and Engineering: A 725 (2018) 406–418.
[14] X. Li, J.J. Shi, G.H. Cao, A.M. Russell, Z.J. Zhou, C.P. Li, G.F. Chen, Improved plasticity of Inconel 718 superalloy fabricated by selective laser melting through a novel heat treatment process, Mater Des 180 (2019) 107915.
[15] J. Schneider, B. Lund, M. Fullen, Effect of heat treatment variations on the mechanical properties of Inconel 718 selective laser melted specimens, Additive Manufacturing 21 (2018) 248–254.
[16] A. Yadollahi, N. Shamsaei, S.M. Thompson, D.W. Seely, Effects of process time interval and heat treatment on the mechanical and microstructural properties of direct laser deposited 316 L stainless steel, Materials Science and Engineering: A 644 (2015) 171–183.
[17] X. Chen, J. Li, X. Cheng, H. Wang, Z. Huang, Effect of heat treatment on microstructure, mechanical and corrosion properties of austenitic stainless steel 316 L using arc additive manufacturing, Materials Science and Engineering: A 715 (2018) 307–314.
[18] Y. Jin, B. Lin, M. Bernacki, G.S. Rohrer, A.D. Rollett, N. Bozzolo, Annealing twin development during recrystallization and grain growth in pure nickel, Materials Science and Engineering: A 597 (2014) 295–303.
[19] S.K. Pradhan, P. Bhuyan, C. Kaithwas, S. Mandal, Strain-Annealing Based Grain Boundary Engineering to Evaluate its Sole Implication on Intergranular Corrosion in Extra-Low Carbon Type 304 L Austenitic Stainless Steel, Metallurgical and Materials Transactions A 49 (7) (2018) 2817–2831.
[20] V. Randle, R. Jones, Grain boundary plane distributions and single-step versus multiple-step grain boundary engineering, Materials Science and Engineering: A 524 (1–2) (2009) 134–142.
[21] F. Bachmann, R. Hielscher, H. Schaeben, Grain detection from 2d and 3d EBSD data–specification of the MTEX algorithm, Ultramicroscopy 111 (12) (2011) 1720–1733.
[22] D.G. Brandon, The structure of high-angle grain boundaries, Acta Metallurgica 14 (11) (1966) 1479–1484.
[23] G.P. Dinda, A.K. Dasgupta, J. Mazumder, Texture control during laser deposition of nickel-based superalloy, Scr Mater 67 (5) (2012) 503–506.
[24] S.-.H. Sun, T. Ishimoto, K. Hagihara, Y. Tsutsumi, T. Hanawa, T. Nakano, Excellent mechanical and corrosion properties of austenitic stainless steel with a unique crystallographic lamellar microstructure via selective laser melting, Scr Mater 159 (2019) 89–93.
[25] H.L. Wei, J. Mazumder, T. DebRoy, Evolution of solidification texture during additive manufacturing, Sci Rep 5 (1) (2015) 16446.
[26] V. Manvatkar, A. De, T. DebRoy, Spatial variation of melt pool geometry, peak temperature and solidification parameters during laser assisted additive manufacturing process, Materials Science and Technology 31 (8) (2015) 924–930.
[27] Y.M. Wang, T. Voisin, J.T. McKeown, J. Ye, N.P. Calta, Z. Li, Z. Zeng, Y. Zhang, W. Chen, T.T. Roehling, R.T. Ott, M.K. Santala, P.J. Depond, M.J. Matthews, A.V. Hamza, T. Zhu, Additively manufactured hierarchical stainless steels with high strength and ductility, Nat Mater 17 (1) (2018) 63–71.
[28] R.E. Napolitano, R.J. Schaefer, The convergence-fault mechanism for low-angle boundary formation in single-crystal castings, J Mater Sci 35 (7) (2000) 1641–1659.
[29] M. Newell, K. Devendra, P.A. Jennings, N. D'Souza, Role of dendrite branching and growth kinetics in the formation of low angle boundaries in Ni–base superalloys, Materials Science and Engineering: A 412 (1) (2005) 307–315.
[30] M. Calcagnotto, D. Ponge, E. Demir, D. Raabe, Orientation gradients and geometrically necessary dislocations in ultrafine grained dual-phase steels studied by 2D and 3D EBSD, Materials Science and Engineering: A 527 (10) (2010) 2738–2746.
[31] A. Kundu, D.P. Field, Influence of plastic deformation heterogeneity on development of geometrically necessary dislocation density in dual phase steel, Materials Science and Engineering: A 667 (2016) 435–443.
[32] J. Jiang, T.B. Britton, A.J. Wilkinson, Evolution of dislocation density distributions in copper during tensile deformation, Acta Mater 61 (19) (2013) 7227–7239.
[33] P.J. Szabó, D.P. Field, B. Jóni, J. Horky, T. Ungár, Bimodal Grain Size Distribution Enhances Strength and Ductility Simultaneously in a Low-Carbon Low-Alloy Steel, Metallurgical and Materials Transactions A 46 (5) (2015) 1948–1957.
[34] J. Humphreys, G.S. Rohrer, A. Rollett, Chapter 7 - Recrystallization of Single-Phase Alloys, in: J. Humphreys, G.S. Rohrer, A. Rollett (Eds.), Recrystallization and Related Annealing Phenomena, 3rd Edition, Elsevier, Oxford, 2017, pp. 245–304.
[35] R.D. Doherty, D.A. Hughes, F.J. Humphreys, J.J. Jonas, D.J. Jensen, M.E. Kassner, W.E. King, T.R. McNelley, H.J. McQueen, A.D. Rollett, Current issues in recrystallization: a review, Materials Science and Engineering: A 238 (2) (1997) 219–274.
[36] U. Scipioni Bertoli, A.J. Wolfer, M.J. Matthews, J.-P.R. Delplanque, J.M. Schoenung, On the limitations of Volumetric Energy Density as a design parameter for Selective Laser Melting, Mater Des 113 (2017) 331–340.
[37] M.H. Farshidianfar, A. Khajepour, A.P. Gerlich, Effect of real-time cooling rate on microstructure in Laser Additive Manufacturing, Journal of Materials Processing Technology 231 (2016) 468–478.
[38] Y. Li, D. Gu, Parametric analysis of thermal behavior during selective laser melting additive manufacturing of aluminum alloy powder, Mater Des 63 (2014) 856–867.
[39] H. Li, J. Guo, K. Huai, H. Ye, Microstructure characterization and room temperature deformation of a rapidly solidified NiAl-based eutectic alloy containing trace Dy, J Cryst Growth 290 (1) (2006) 258–265.
[40] T.F. Broderick, A.G. Jackson, H. Jones, F.H. Froes, The effect of cooling conditions on the microstructure of rapidly solidified Ti-6Al-4 V, Metallurgical Transactions A 16 (11) (1985) 1951–1959.
[41] D. Lin, L. Xu, H. Jing, Y. Han, L. Zhao, F. Minami, Effects of annealing on the structure and mechanical properties of FeCoCrNi high-entropy alloy fabricated via selective laser melting, Additive Manufacturing 32 (2020) 101058.
[42] Y. Liu, Y. Yang, D. Wang, A study on the residual stress during selective laser melting (SLM) of metallic powder, The International Journal of Advanced Manufacturing Technology 87 (1) (2016) 647–656.
[43] N.C. Levkulich, S.L. Semiatin, J.E. Gockel, J.R. Middendorf, A.T. DeWald, N.W. Klingbeil, The effect of process parameters on residual stress evolution and distortion in the laser powder bed fusion of Ti-6Al-4 V, Additive Manufacturing 28 (2019) 475–484.
[44] W.M. Steen, J. Mazumder, Laser Surface Treatment, Springer London, London, 2010, pp. 295–347.
[45] K.G. Prashanth, J. Eckert, Formation of metastable cellular microstructures in selective laser melted alloys, J Alloys Compd 707 (2017) 27–34.
[46] L. Liu, Q. Ding, Y. Zhong, J. Zou, J. Wu, Y.-.L. Chiu, J. Li, Z. Zhang, Q. Yu, Z. Shen, Dislocation network in additive manufactured steel breaks strength–ductility trade-off, Materials Today 21 (4) (2018) 354–361.
[47] Y. Hao, J. Li, X. Li, W. Liu, G. Cao, C. Li, Z. Liu, Influences of cooling rates on solidification and segregation characteristics of Fe-Cr-Ni-Mo-N super austenitic stainless steel, Journal of Materials Processing Technology 275 (2020) 116326.
[48] W. Kurz, D. Fisher, Fundamentals of Solidification: fourth Revised Edition, Retrospective Collection (1998).
[49] B. Zheng, Y. Zhou, J.E. Smugeresky, J.M. Schoenung, E.J. Lavernia, Thermal Behavior and Microstructure Evolution during Laser Deposition with Laser-Engineered Net Shaping: part II. Experimental Investigation and Discussion, Metallurgical and Materials Transactions A 39 (9) (2008) 2237–2245.
[50] M. Ma, Z. Wang, X. Zeng, A comparison on metallurgical behaviors of 316 L stainless steel by selective laser melting and laser cladding deposition, Materials Science and Engineering: A 685 (2017) 265–273.
[51] Y. Li, K. Chen, R.L. Narayan, U. Ramamurty, Y. Wang, J. Long, N. Tamura, X. Zhou, Multi-scale microstructural investigation of a laser 3D printed Ni-based superalloy, Additive Manufacturing (2020) 101220.
[52] H. Mughrabi, Deformation-induced long-range internal stresses and lattice plane misorientations and the role of geometrically necessary dislocations, Philosophical Magazine 86 (25–26) (2006) 4037–4054.
[53] O. Rezvanian, M.A. Zikry, A.M. Rajendran, Statistically stored, geometrically necessary and grain boundary dislocation densities: microstructural representation and modelling, Proceedings of the Royal Society A: mathematical, Physical and Engineering Sciences 463 (2087) (2007) 2833–2853.

[54] D. Guan, W.M. Rainforth, L. Ma, B. Wynne, J. Gao, Twin recrystallization mechanisms and exceptional contribution to texture evolution during annealing in a magnesium alloy, Acta Mater 126 (2017) 132–144.
[55] A. Marandi, R. Zarei-Hanzaki, A. Zarei-Hanzaki, H.R. Abedi, Dynamic recrystallization behavior of new transformation–twinning induced plasticity steel, Materials Science and Engineering: A 607 (2014) 397–408.
[56] S.L. Sobolev, Local non-equilibrium diffusion model for solute trapping during rapid solidification, Acta Mater 60 (6) (2012) 2711–2718.
[57] C. Slater, A. Mandal, C. Davis, The Influence of Segregation of Mn on the Recrystallization Behavior of C-Mn Steels, Metallurgical and Materials Transactions B 50 (4) (2019) 1627–1636.
[58] N. Stanford, D. Atwell, M.R. Barnett, The effect of Gd on the recrystallisation, texture and deformation behaviour of magnesium-based alloys, Acta Mater 58 (20) (2010) 6773–6783.
[59] R. Ding, Y. Yao, B. Sun, G. Liu, J. He, T. Li, X. Wan, Z. Dai, D. Ponge, D. Raabe, C. Zhang, A. Godfrey, G. Miyamoto, T. Furuhara, Z. Yang, S. van der Zwaag, H. Chen, Chemical boundary engineering: a new route toward lean, ultrastrong yet ductile steels, Sci Adv 6 (13) (2020) eaay1430.
[60] S.G. Kim, Y.B. Park, Grain boundary segregation, solute drag and abnormal grain growth, Acta Mater 56 (15) (2008) 3739–3753.
[61] A. Das, Revisiting Stacking Fault Energy of Steels, Metallurgical and Materials Transactions A 47 (2) (2016) 748–768.
[62] Y. Hong, C. Zhou, Y. Zheng, L. Zhang, J. Zheng, X. Chen, B. An, Formation of strain-induced martensite in selective laser melting austenitic stainless steel, Materials Science and Engineering: A 740-741 (2019) 420–426.
[63] R.E. Schramm, R.P. Reed, Stacking fault energies of seven commercial austenitic stainless steels, Metallurgical Transactions A 6 (7) (1975) 1345.
[64] B. Song, S. Dong, Q. Liu, H. Liao, C. Coddet, Vacuum heat treatment of iron parts produced by selective laser melting: microstructure, residual stress and tensile behavior, Materials & Design (1980-2015) 54 (2014) 727–733.
[65] B. Clausen, T. Lorentzen, T. Leffers, Self-consistent modelling of the plastic deformation of f.c.c. polycrystals and its implications for diffraction measurements of internal stresses, Acta Mater 46 (9) (1998) 3087–3098.
[66] S. Guan, D. Wan, K. Solberg, F. Berto, T. Welo, T.M. Yue, K.C. Chan, Additively manufactured CrMnFeCoNi/AlCoCrFeNiTi0.5 laminated high-entropy alloy with enhanced strength-plasticity synergy, Scr Mater 183 (2020) 133–138.
[67] X. Wu, M. Yang, F. Yuan, G. Wu, Y. Wei, X. Huang, Y. Zhu, Heterogeneous lamella structure unites ultrafine-grain strength with coarse-grain ductility, Proceedings of the National Academy of Sciences 112 (47) (2015) 14501.